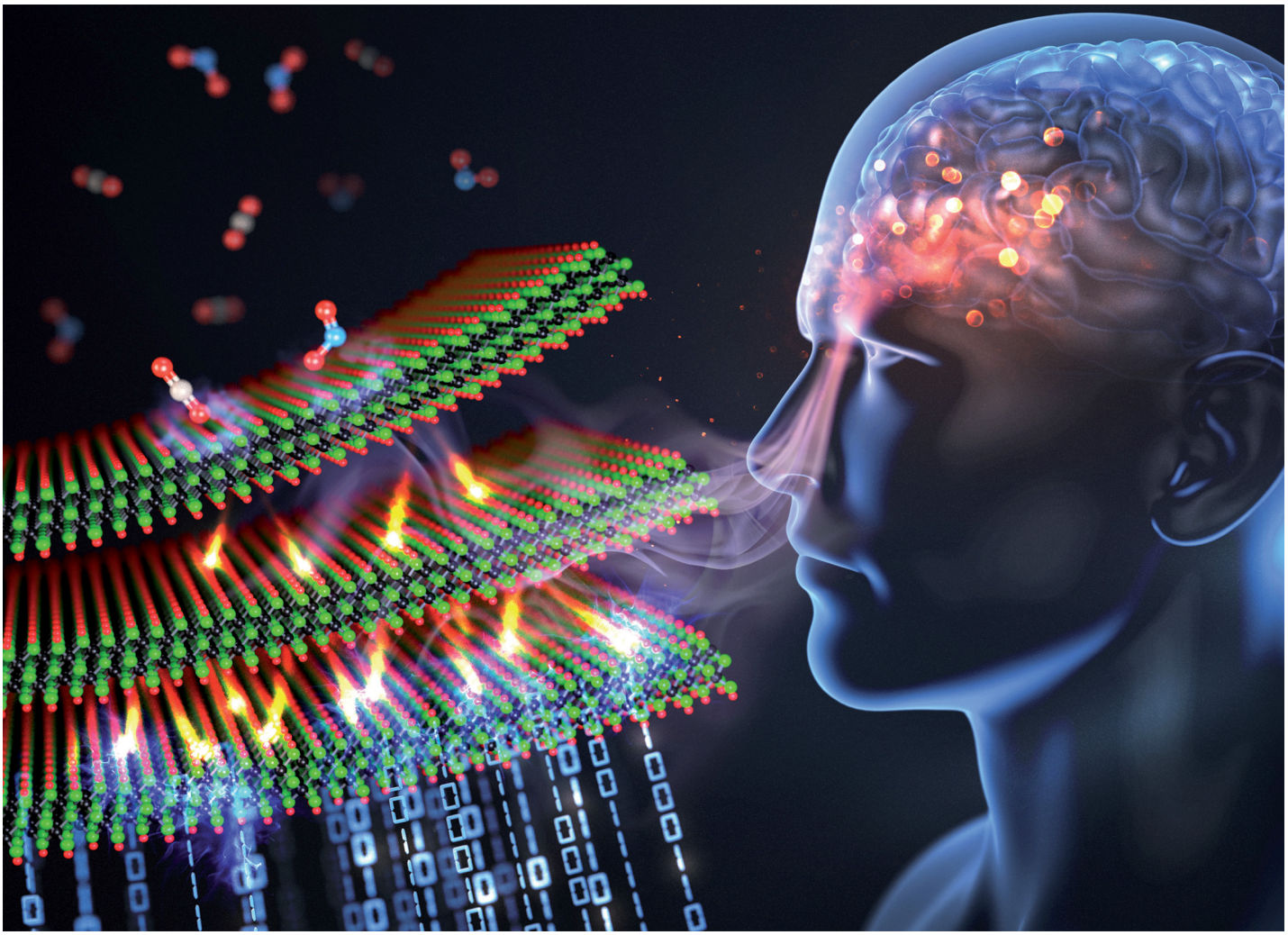

Exhibiting research from Professor Jun Hong Park's group at Bio-inspired Semiconductor laboratory, Gyeongsang National University, Jinju-si, South Korea.

Chemically configurable analogue memristors, *via* the chemiresistive response of oxidized MXene

The integration of gas sensing and neuromorphic computing within a single device presents a transformative architecture for artificial olfaction and edge-level intelligent perception, enabling simultaneous sensing and computation on a unified platform.

Image reproduced by permission of Jun Hong Park from *Mater. Horiz.*, 2025, **12**, 5677.

As featured in:

See Sang Yong Nam, Jun Hong Park *et al.*, *Mater. Horiz.*, 2025, **12**, 5677.

ROYAL SOCIETY OF CHEMISTRY

rsc.li/materials-horizons

Registered charity number: 207890

Materials Horizons

ROYAL SOCIETY OF CHEMISTRY

COMMUNICATION

View Article Online
View Journal | View Issue

Cite this: *Mater. Horiz.*, 2025, **12**, 5677

Received 2nd May 2025,
Accepted 6th June 2025

DOI: 10.1039/d5mh00834d

rsc.li/materials-horizons

Chemically configurable analogue memristors, *via* the chemiresistive response of oxidized MXene†

Somnath S. Kundale,‡[ab] Muhammad Abubakr,‡[a] Jihye Park,‡[a] Fernando Ordonez Morales,[a] I Ketut Gary Devara,[a] Windy Ayu Lestari,[a] Riya Chatterjee,[a] Sang Yong Nam *[ab] and Jun Hong Park *[ab]

The integration of gas sensing and neuromorphic computing within a single device offers a transformative architecture for artificial olfaction and edge-level intelligent perception. In this study, we demonstrate the feasibility of analogue chemiresistive memristors with an Au/oxidized MXene/Au structure for multifunctional operation. The hydrothermally oxidized MXene, rich in active sites favorable for redox reactions, enables modulation of conductance states *via* CO_2 and NO_2 gas adsorption on its surface. This dual electrical and molecular tuning yields distinctly separable conductance states, essential for emulating artificial synaptic functions. The device exhibits clear analogue resistive switching and both volatile and non-volatile memory behaviors under electrical and molecular stimuli, indicative of reliable synaptic plasticity. Moreover, gas exposure induces electrical potentiation and depression of conductance states, replicating key features of olfactory synaptic behavior. Its dynamic response to gas pulses, long-term retention, and pulse-dependent plasticity highlight its ability to store and process environmental chemical stimuli in real time. To validate its neuromorphic computing capability, an artificial neural network (ANN) was implemented using the digit-MNIST and fashion-MNIST datasets, achieving recognition accuracies of 95% and 82%, respectively. These results confirm the potential for integrated sensing and computation on a single platform.

New concepts

This study presents a conceptual advance by engineering oxidized MXene-based chemiresistive memristors that integrate molecular detection and neuromorphic computing within a single platform. Unlike conventional gas sensors or memristors, our approach leverages oxidation-induced active surface sites in MXene to achieve conductance modulation in response to CO_2 gas adsorption. This allows dynamic switching between multiple, separable conductance states, an essential feature for mimicking biological synapses. Importantly, we demonstrate stable molecular dynamics dependent synaptic behavior and analog memory functionalities through gas-triggered conductance retention tests, addressing scalability and stability challenges for practical olfactory systems. Further, the device's neuromorphic performance was validated by integrating it into an artificial neural network (ANN), achieving 95% and 82% accuracy on digit MNIST and fashion-MNIST datasets, respectively. This work introduces oxidized MXene as a dual-functional material for gas sensing and neuromorphic memory. It highlights its critical role in enabling scalable, bioinspired sensory-inference systems, offering a transformative path forward for artificial intelligence hardware based on material innovations.

1. Introduction

The rapid advancements in industrialization and urbanization have led to a significant increase in environmental pollution,[1] primarily through the emission of toxic gases such as nitrogen dioxide (NO_2), ammonia (NH_3), nitrogen monoxide (NO), and carbon dioxide (CO_2).[2,3] Among these, NO_2 plays a critical role in enhancing urban carbon emission assessments by enabling the differentiation between anthropogenic and biogenic CO_2 sources.[4] These gases, largely released from industrial operations and vehicular exhaust, contribute substantially to air pollution and its associated detrimental effects.[5] The presence of such hazardous gases poses serious risks to both human health and the environment, necessitating their accurate detection and continuous monitoring to ensure public safety.[6]

Chemiresistive sensors have emerged as a widely adopted solution for real-time gas monitoring due to their ability to safeguard human health and ecosystems.[7] Their high selectivity, sensitivity, simple device architecture, compact form, low operating temperature, and minimal power requirements make them indispensable in industrial, environmental, and medical applications.[8,9] These sensors function by detecting resistance changes in the active channel layer upon exposure to target

[a] *Department of Materials Engineering and Convergence Technology, Gyeongsang National University, Jinju, Gyeongsangnam-do 52828, Republic of Korea. E-mail: walden@gnu.ac.kr, yakte@gnu.ac.kr*

[b] *Research Institute for Green Energy Convergence Technology, Gyeongsang National University, Jinju, Gyeongsangnam-do 52828, Republic of Korea*

† Electronic supplementary information (ESI) available. See DOI: https://doi.org/10.1039/d5mh00834d

‡ These authors contributed equally.

gases, with performance dependent on both the material properties and the specific analyte. However, achieving enhanced chemical sensitivity remains a critical challenge, particularly for detecting ultralow concentrations of analytes. One effective approach to improve sensitivity involves reducing the thickness of the active layer. In response, researchers have explored a wide range of nanomaterials as active sensing layers in chemiresistive gas sensors. Various materials, including metal oxides, conductive polymers, and carbon-based nanostructures like nanotubes, have been extensively investigated, In recent decades, metal oxides have attracted considerable interest due to their excellent potential in sensing applications.[10]

MXene, a two-dimensional transition metal carbide or nitride, has recently emerged as a promising material of interest garnered significant attention due to its exceptional electrical conductivity and surface functionalization capabilities.[11] Its large surface area, adjustable surface functionalities and robust structural integrity position it as a strong contender for gas sensing technologies.[12] However, pristine MXenes suffer from limited gas sensing performance this is mainly attributed to the absence of targeted functional moieties, limited bandgap, and insufficient mechanical robustness.[13] In contrast, oxidized MXene-based sensors have shown significant potential for enhanced gas detection, owing to their ability to readily transform into TiO_2. The anatase phase of TiO_2, in particular, offers high redox potential and its remarkable resistance to thermal and chemical degradation renders it highly suitable for gas sensing purposes.

Concurrently, the field of neuromorphic engineering has been advancing efforts to emulate the information processing capabilities of the human brain in electronic systems.[14] Inspired by the biological somatosensory system, which detects and processes external stimuli, researchers have been developing artificial sensory systems capable of mimicking neural responses.[15] Notably, integrating gas sensors with neuromorphic architectures represents an emerging paradigm in bioinspired computing, enabling sensors not only to detect stimuli but also to exhibit memory-like behavior akin to biological synapses.[16] This strategy opens pathways toward artificial olfactory systems capable of both sensing and memorizing gas inputs. However, conventional gas sensors face significant limitations, including slow response and recovery times, and the inability to integrate sensing and memory functionalities within a single device.[17] To overcome these limitations, novel sensors with memristive properties are being explored. These devices can modulate their conductance through redox reactions, offering a promising route to realize artificial olfactory synapses.[18]

In this study, we present the development of an oxidized MXene-based chemiresistive memristor that not only delivers exceptional sensitivity to trace-level gases but also exhibits synaptic behavior through both electrical and gas-induced conductance modulation. The proposed Au/oxidized MXene/Au device demonstrates high sensitivity, reproducibility, and repeatability. It combines the advantages of the Schottky behavior of oxidized MXenes for enhanced gas detection with the memristive properties required to emulate biological synapses. By integrating these dual functionalities into a single platform, we establish a new paradigm for chemiresistive memristors capable of both sensing and memorizing gas stimuli, thereby contributing to the advancement of neuromorphic engineering. To further assess its computational potential, we implemented an artificial neural network (ANN) using the digit MNIST and fashion-MNIST datasets. This study lays the foundation for advancing of intelligent gas-sensing devices that mimic human olfactory responses, with broad applications in environmental monitoring and bioinspired computing.

2. Results and discussion

To synthesize MXene, the Al layer was selectively etched from Ti_3AlC_2 (MAX phase) using a pre-mixed hydrofluoric acid (HF) solution for 18 h, following established procedures.[19] For subsequent oxidation, the obtained $Ti_3C_2T_x$ was dispersed in a mixture of deionized water and H_2O_2, then subjected to hydrothermal processing at 180 °C for 12 h. Fig. 1(a) schematically illustrates the etching and oxidation processes.

The surface morphologies of the synthesized and oxidized MXene were characterized using scanning electron microscopy (SEM), and the elemental compositions were investigated through energy-dispersive X-ray spectroscopy (EDS). Fig. 1(b) shows an SEM image of $Ti_3C_2T_x$, revealing a loosely stacked layered structure typical of MXene obtained by selective etching of the MAX phase.[20] The corresponding EDS mapping confirms the presence of fluorine (F), oxygen (O), titanium (Ti), and carbon (C). Fig. 1(c) presents the surface of oxidized MXene, where hydrothermal process in the presence H_2O_2 and atmospheric oxygen and moisture leads to the formation of TiO_2 due to the interaction of surface functional groups (OH, O, and F) with the environment.[21] The EDS mapping indicates a marked increase in oxygen content, this confirmed the uniform deposition of TiO_2 on the MXene surface.

To analyze the crystalline structures of pristine and oxidized $Ti_3C_2T_x$, X-ray diffraction (XRD) and Raman spectroscopy were performed. A detailed analysis of the crystallographic and vibrational characteristics is provided in Fig. S1 and discussed in the ESI.† Field-emission transmission electron microscopy (FE-TEM) was utilized to characterize the nanoscale structural evolution of MXene during oxidation. TEM images of pristine MXene (Fig. 1(d) to (f)) reveal a layered morphology, with stacked nanosheets clearly visible in Fig. 1(e). The high-resolution TEM image in Fig. 1(f) reveals as a lattice fringe spacing of 0.25 nm, corresponding to the (111) plane of $Ti_3C_2T_x$.[22] In contrast, TEM images of oxidized MXene (Fig. 1(g) to (i)) exhibit the coexistence of $Ti_3C_2T_x$ and TiO_2 phases. Specifically, Fig. 1(i) reveals two distinct lattice spacings of 0.25 nm and 0.35 nm, corresponding to the (111) plane of $Ti_3C_2T_x$ and the (101) plane of anatase TiO_2, respectively.[23]

The chemical states and bonding configurations of pristine and oxidized MXene were investigated using X-ray photoelectron spectroscopy (XPS), as shown in Fig. 2. Survey and

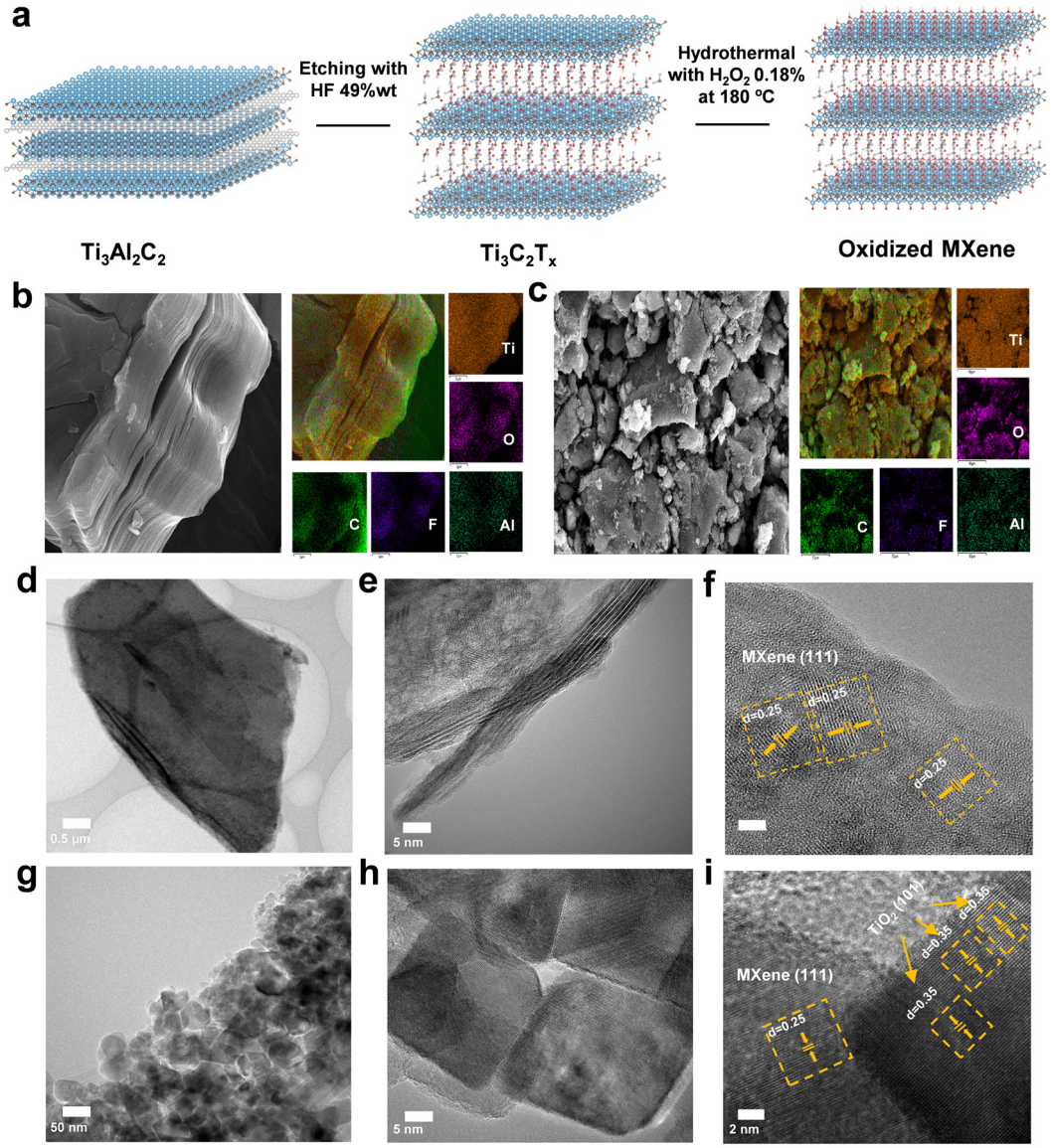

Fig. 1 (a) Schematic illustration of the synthesis of MXene from the MAX phase followed by hydrothermal oxidation to obtain oxidized MXene. (b) Scanning electron microscopy (SEM) image and energy-dispersive X-ray spectroscopy (EDS) elemental mapping of pristine MXene. (c) SEM image and EDS elemental mapping of oxidized MXene. Microstructural characterization of pristine and oxidized MXene. (d) and (g) Field-emission transmission electron microscopy (FE-TEM) images, (e) and (h) magnified TEM images, and (f) and (i) high-resolution TEM (HR-TEM) images.

quantitative elemental analysis confirmed the presence of Ti, C, O, and F in both samples, consistent with the EDS findings (see Fig. S2 in the ESI†). The Ti 2p spectrum of pristine MXene (Fig. 2(a)) was deconvoluted into distinct peaks at 464.1 eV (Ti–C), 461.1 eV (Ti–F), and 458.2 eV (TiO_2), along with oxidation states at 455.0 eV (Ti(I)), 455.5 eV (Ti(II)), and 456.4 eV (Ti(III)).[24–26] These peaks signify Ti–T_x bonds, where T represents surface terminations group such as O, OH, or F.[27,28] The C 1s spectrum (Fig. 2(b)) exhibited peaks at 282.15 eV (C–Ti), 284.8 eV (C═C), 287.0 eV (C–O), and 288.5 eV (O–C═O), while the O 1s spectrum (Fig. 2(c)) exhibited peaks at 529.9 eV (TiO_2), 531.2 eV (O–H), and 532.9 eV (C–O), confirming Ti–OH bonding and the formation of $Ti_3C_2(OH)_x$.[29,30]

In oxidized MXene, the Ti 2p spectrum (Fig. 2(d)) exhibited peaks at 458.6, 464.4, 471.9, and 477.8 eV, attributed to Ti(I), TiO_2, Ti(III), and Ti–O species, respectively.[31–33] The disappearance of Ti–F and Ti–C peaks, accompanied by a stronger TiO_2 signal, indicates substantial oxidation. The C 1s spectrum (Fig. 2(e)) exhibited the absence of the C–Ti peak and the presence of C–C, C–O, and O–C═O bonds, suggesting the formation of amorphous carbon. Additionally, the O 1s spectrum (Fig. 2(f)) revealed a prominent TiO_2 peak, further confirming the conversion of MXene into TiO_2 and carbonaceous phases upon oxidation.[34]

Chemiresistive sensors were fabricated by drop-casting oxidized MXene onto a SiO_2/Si substrate, and then gold electrodes

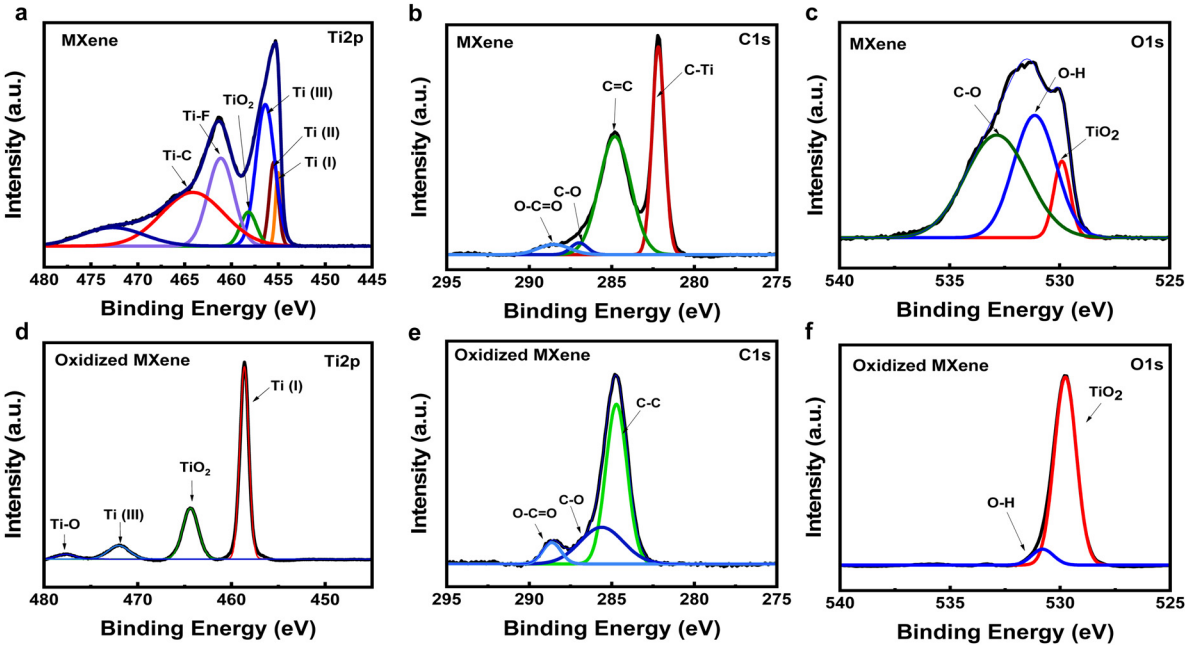

Fig. 2 X-ray photoelectron spectroscopy (XPS) analysis of pristine MXene: (a) Ti 2p, (b) C 1s, and (c) O 1s spectra; and oxidized MXene: (d) Ti 2p, (e) C 1s, and (f) O 1s spectra.

were deposited on top using e-beam evaporation. Fig. 3(a) illustrates the device architecture, highlighting the interdigitated Au electrodes. The *I–V* characteristics of the pristine MXene sensor (Fig. 3(b)) exhibited a linear response within the −10 to +10 V range, indicating Ohmic contact between MXene and the Au electrodes, with a resistance of $1.37 \times 10^3\ \Omega$. In contrast, the oxidized MXene sensor demonstrated non-linear *I–V* behavior (Fig. 3(c)), characteristic of a Schottky barrier. The oxidation process significantly reduced the electrical conductivity of MXene, resulting in a high resistance of $18.37 \times 10^6\ \Omega$ at room temperature. This substantial increase in resistance and the emergence of Schottky behavior are attributed to the formation and incorporation of TiO_2 within the MXene matrix.[35]

The gas sensing performance of pristine and oxidized MXene was assessed at room temperature. As shown in Fig. S3 (ESI†), both sensors exhibited a decrease in current upon exposure to 10 ppm of CO_2 and NO_2, with detailed explanations provided in the ESI.† The conductance returns to baseline after gas exposure ceases, indicating the desorption of gas molecules from the oxidized MXene surface. This behavior confirms the reversible nature of gas adsorption–desorption processes, which is crucial for the stability and durability of chemiresistive sensors.[36,37] Fig. 3(d) displays the normalized current response ($\Delta I/I_0$) of the pristine and oxidized MXene chemiresistive sensor for NO_2, while Fig. 3(e) shows the corresponding response for the pristine and oxidized MXene chemiresistive sensor upon exposure to 15 ppm of CO_2. Each gas was introduced for 50 s, during which the *I–V* characteristics were continuously recorded. All measurements were conducted in a vacuum probe chamber maintained at a base pressure of 5×10^{-6} torr. The chemiresistive sensor exhibits a slight decrease in current response over time (up to 150 s) during continuous exposure to 10 ppm CO_2, highlighting its persistent sensing capability under prolonged CO_2 conditions (see Fig. S4, ESI†). This may result from the slow desorption of CO_2 molecules from the oxidized MXene surface at 300 K.[38,39] The chemiresistive sensor response was quantitatively evaluated using eqn (1).[40]

$$\text{Response}\,(\%) = \frac{\Delta I}{I_0} \times 100\% = \frac{I_g - I_0}{I_0} \times 100\% \qquad (1)$$

here, I_g represents the current measured during gas exposure, while I_0 denotes the baseline current without gas exposure. Here, ΔI is the absolute current response extracted from I_g and I_0. The pristine MXene chemiresistive sensor exhibited responses ($\Delta I/I_0$) of 0.11 for NO_2 and 0.046 to CO_2, while the oxidized MXene sensor exhibited significantly higher responses of 0.85 and 1.41, respectively. Here ΔI is absolute current response. The lower response observed for pristine MXene in this study, compared to our previous work, is primarily attributed to differences in surface area and morphology arising from a shorter etching duration for 18 h in the present study *versus* etched MXene for 24 h previously.[19] These results suggest that the incorporation of TiO_2 into the MXene structure alters its electronic properties and increases surface reactivity, thereby enhancing gas adsorption and desorption dynamics and overall sensing performance.[35]

The signal-to-noise ratio (SNR) of both pristine MXene and oxidized MXene sensors for NO_2 and CO_2 was evaluated by comparing their response magnitudes with baseline noise, as shown in Fig. S5 (ESI†) and explained in the ESI.† Response

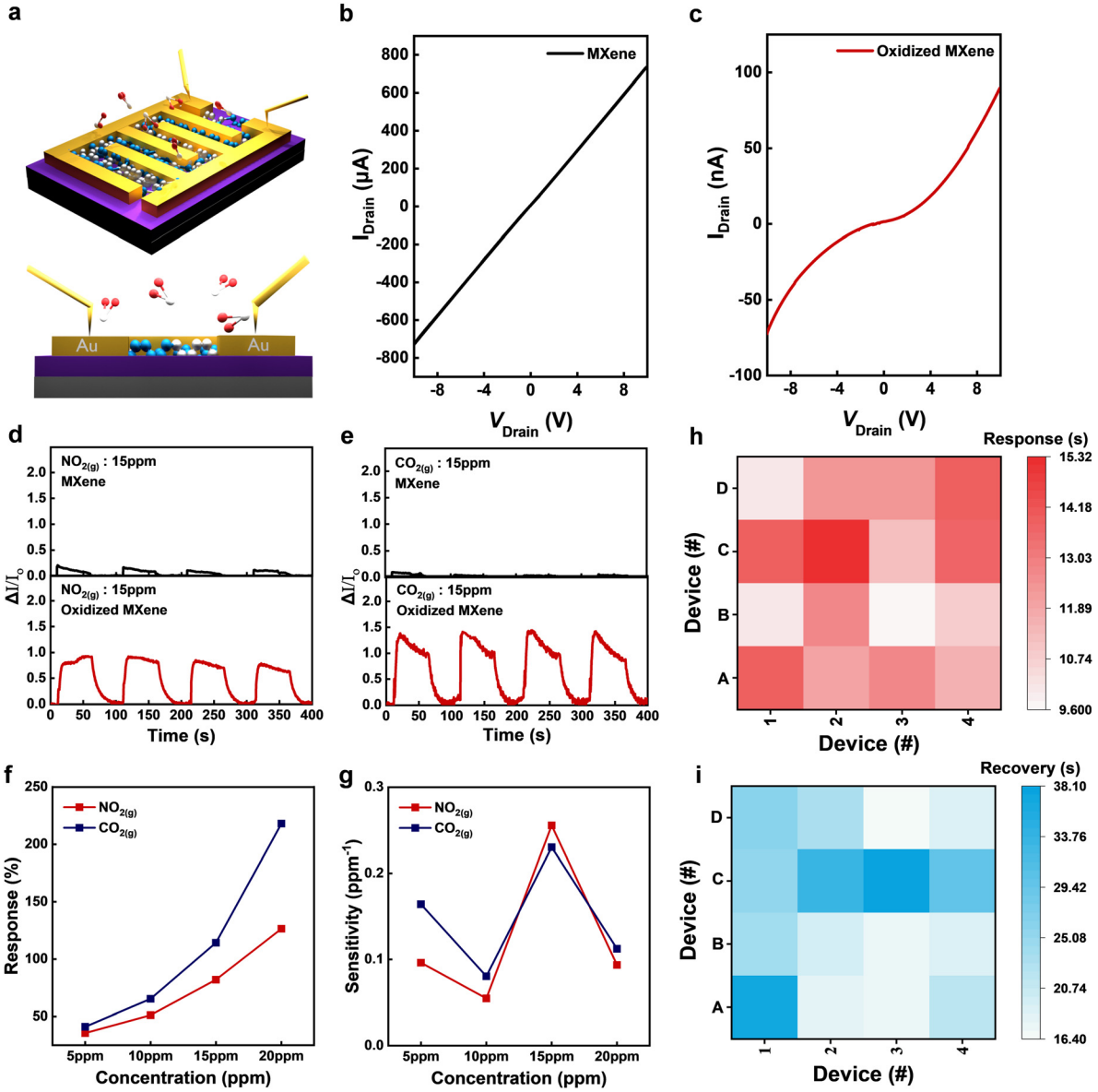

Fig. 3 (a) Schematic illustration of the chemiresistive sensor structure. Current–voltage (I–V) characteristics of (b) pristine MXene and (c) oxidized MXene. Repeatability of sensor responses, showing current variation ($\Delta I/I_0$) during repeated 50 s exposure and recovery cycles to (d) NO_2 and (e) CO_2. (f) Maximum response and (g) sensitivity of oxidized MXene chemiresistive sensors to NO_2 and CO_2 concentrations ranging from 5 to 20 ppm. (h) Response time and (i) recovery time of all fabricated devices.

and recovery times of the MXene and oxidized MXene chemiresistive sensors for 15 ppm NO_2 and CO_2 exposures are provided in Fig. S6 (ESI†).

The Fig. 3(f) and (g) summarize the maximum response and sensitivity trends of the oxidized MXene sensor across varying concentrations of CO_2 and NO_2. As illustrated in Fig. 3(f), the sensor shows maximum responses of 35.6%, 51.2%, 82%, and 126.5% for NO_2, and 41.1%, 65.3%, 114.3%, and 218% for CO_2 at concentrations of 5, 10, 15, and 20 ppm, respectively. These values reflect superior sensitivity toward both analytes compared to our previously reported MXene/lignin-based device.[19] The sensitivity (S) of the oxidized MXene chemiresistive sensors was calculated using eqn (2).[41]

$$S(\mathrm{ppm}^{-1}) = \frac{\Delta R}{\Delta C} \quad (2)$$

here, ΔR represents the change in the chemiresistive sensor response, while ΔC indicates the change in gas concentration. Compared to pristine MXene, the oxidized MXene chemiresistive sensors exhibited significantly higher sensitivities of 0.26 and 0.23 for 15 ppm NO_2 and CO_2, respectively. These results are consistent with the sensor responses shown in Fig. 3(g), further confirming the enhanced gas sensing performance of oxidized MXene.

To evaluate fabrication reliability, device-to-device variations in response and recovery times were analyzed across 16 oxidized MXene chemiresistive sensors, as depicted in Fig. 3(h) and (i). Notably, approximately 80% of the sensors achieved response times under 13 s and recovery times below 25 s. This high level of consistency highlights the reproducibility and robustness of the fabrication method, underscoring its promise for scalable and practical sensing applications.[42] The reproducibility of the oxidized MXene chemiresistive sensor was further assessed for performance stability, as shown in ESI† Fig. S7. Fig. S8 (ESI†) presents the repeatable gas sensing behavior of the oxidized MXene sensors for NO_2 and CO_2 concentrations ranging from 5 to 20 ppm.

As chemiresistive sensor technologies advance toward mimicking biological perception, simple detection is no longer sufficient. These devices must also demonstrate neuromorphic learning behavior in response to external stimuli.[43] In this study, we fabricated an oxidized MXene-based chemiresistive memristor device that integrates both sensing and synaptic functionalities into a single platform. The Au/oxidized MXene/Au device architecture is illustrated in Fig. 4(a). From inspired by the human olfactory system, where sensory detection and memory formation are governed by neural processing (Fig. 4(b)), our device seeks to emulate integrated perception and memory behavior upon CO_2 exposure.[44] Analogue resistive switching is preferred for neuromorphic computing applications, as it enables gradual conductance modulation, in contrast to digital switching which is typically used for memory storage.[45] In analogue switching, conductance increases progressively in response to pulsed electrical stimuli, offering more nuanced control compared to the abrupt transitions in digital switching.[46] Motivated by this, we achieved analogue-type resistive switching in the fabricated chemiresistive memristor, characterized by smooth and linear conductance modulation with good linearity, which is essential feature for efficient neuromorphic functionality.

The electrical behavior of the chemiresistive memristor was first evaluated through current–voltage (*I–V*) measurements. It exhibited analogue *I–V* characteristics with significantly enhanced current responses at ±5 V, identified as the optimal operating voltage. Fig. 4(c) presents the *I–V* characteristics under vacuum and upon exposure to 15 ppm NO_2 and CO_2. In both cases, a decrease in current was observed, attributed to increased resistance from gas adsorption on the sensing layer. Notably, CO_2 exposure resulted in a more substantial current decrease than NO_2, indicating stronger interaction between CO_2 molecules and the oxidized MXene surface. This observation aligns with our gas sensing data and confirms the higher affinity of CO_2 toward oxidized MXene.[47] To assess memory retention a key requirement in neuromorphic systems we evaluated the stability of conductance states under gas exposure. Fig. 4(d) and (e) show the retention behavior at various concentrations of NO_2 and CO_2, respectively, at a read voltage of 0.2 V. The observed low current range is attributed to the application of a low read voltage. While NO_2 exposure led to greater fluctuations in conductance states, CO_2 exposure resulted in more stable and well-separated states, yielding a significantly wider and more reliable memory window, defined as the difference between the low-resistance state (LRS), representing the baseline resistance under vacuum conditions, and the high-resistance state (HRS) triggered by varying concentrations of NO_2 and CO_2. The LRS/HRS ratio increased from 3 under 15 ppm NO_2 to 4.1 under 15 ppm CO_2, highlighting the enhanced response of the device to CO_2. Based on these promising results, subsequent measurements focused exclusively on CO_2.

Subsequently, we explored both electrically and molecularly triggered synaptic behavior by employing CO_2 gas as a neuromodulatory agent. Initially, we investigated the potentiation and depression characteristics of the Au/oxidized MXene/Au device under electrical stimulation in the presence of CO_2 exposure. Fig. 4(f) illustrates the excitatory postsynaptic current (EPSC) responses under vacuum and CO_2 concentrations ranging from 5 to 15 ppm. The measurements were conducted by applying a train of 20 consecutive voltage pulses (5 V amplitude, 20 μs pulse width). The results reveal a gradual decrease in EPSC amplitude as CO_2 concentration increases from 5 ppm to 15 ppm, indicating a concentration-dependent modulation of synaptic potentiation. Notably, the operating range of potentiation in vacuum conditions is higher than under gas exposure.

Similarly, inhibitory postsynaptic current (IPSC) responses, which reflect synaptic depression, were measured under the same pulse conditions and are shown in Fig. 4(g). A similar trend is observed, where the IPSC amplitude progressively decreases with increasing CO_2 concentrations, further highlighting the modulatory effect of CO_2 on synaptic dynamics. These findings clearly demonstrate that CO_2 not only influences the conductance states of the device but also actively modulates synaptic plasticity, including both potentiation and depression. Motivated by these results, we further investigated the possibility of inducing synaptic behavior through gas pulses alone, aiming to assess the intrinsic neuromorphic response of the device under exclusive CO_2 stimulation.

The distance-dependent gas sensing response is a crucial performance parameter for both conventional gas sensors and gas-triggered neuromorphic devices.[48] However, several previous studies have primarily focused on the proximity between the gas source and the sensing device, often neglecting a comprehensive evaluation of how distance affects sensing performance.[49] This oversight presents significant challenges for the commercialization of such devices, where reliable and consistent sensing across varying distances is essential. To address this limitation, we systematically measured and compared the gas-dependent responses of both lateral and sandwiched device configurations, as shown in Fig. 5.

Distance sensitivity exposure 15 ppm CO_2 was further evaluated by varying the distance between the gas source and the chemiresistive sensor, as depicted in Fig. 5(a). Fig. 5(b) presents the current responses of the oxidized MXene chemiresistive sensor exposed to 15 ppm CO_2 at distances ranging from 1 to 5 cm. As the distance increased, the sensor response decreased from 1.88 to 1.10 owing to the reduced impingement rate of gas

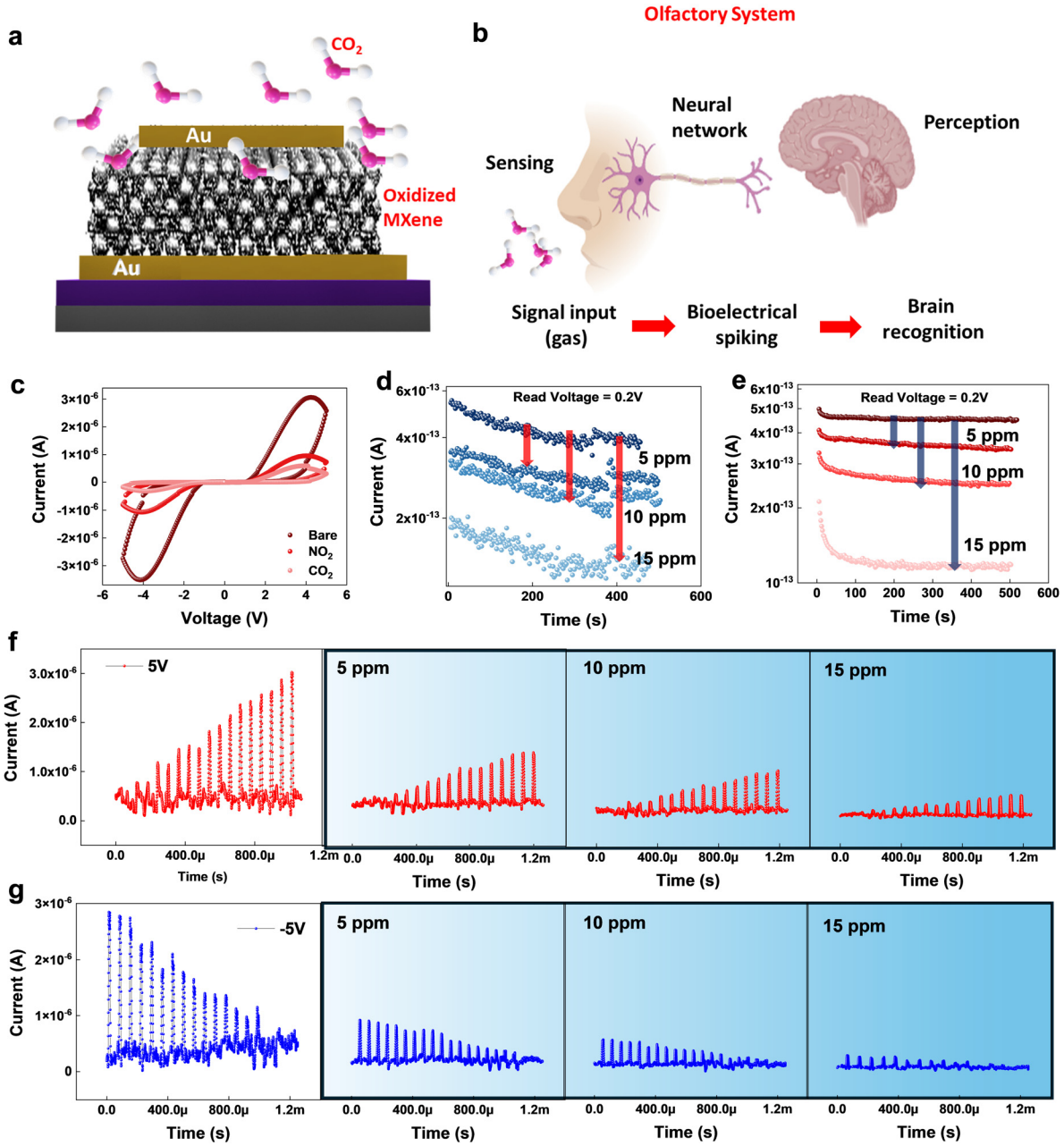

Fig. 4 (a) Schematic illustration of the Au/oxidized MXene/Au chemiresistive memristor device architecture for gas-triggered neuromorphic applications. (b) Conceptual schematic of the human olfactory system, illustrating the processes of sensing and learning. (c) *I–V* characteristics of the fabricated device under vacuum and upon exposure to 15 ppm NO_2 and CO_2 at ±5 V. (d) Retention of conductance states under vacuum and upon exposure to 5, 10, and 15 ppm NO_2 at 0.2 V. (e) Retention of conductance states under vacuum and upon exposure to 5, 10, and 15 ppm CO_2 at 0.2 V. (f) EPSC response of the Au/oxidized MXene/Au chemiresistive memristor in vacuum and at various concentrations of CO_2 (15 ppm). (g) IPSC response of the Au/oxidized MXene/Au chemiresistive memristor in vacuum and at various concentrations of CO_2 (15 ppm).

molecules on the sensor surface.[50] Fig. 5(c) summarizes the maximum responses, with values of 188.5%, 146.6%, 132.4%, 122.8%, and 110.5% at distances of 1, 2, 3, 4, and 5 cm, respectively, confirming a clear distance-dependent sensitivity.

From a neuromorphic perspective, we investigated the distance-dependent *I–V* characteristics of the vertical device structure under a ±5 V bias, as shown in Fig. 5(d). A similar trend was observed as in the lateral devices, with both the overall current range and hysteresis area progressively increasing as the distance between the gas source and the device grew. This trend suggests that CO_2 affinity at low proximity increases resistance. Fig. 5b presents the normalized response in the form of $\Delta I/I_0$, (where ΔI is the absolute current response extracted from I_g and I_0) measured using a planar interdigitated electrode device configuration. In this case, although the actual current continues to increase, the relative response ($\Delta I/I_0$) tends

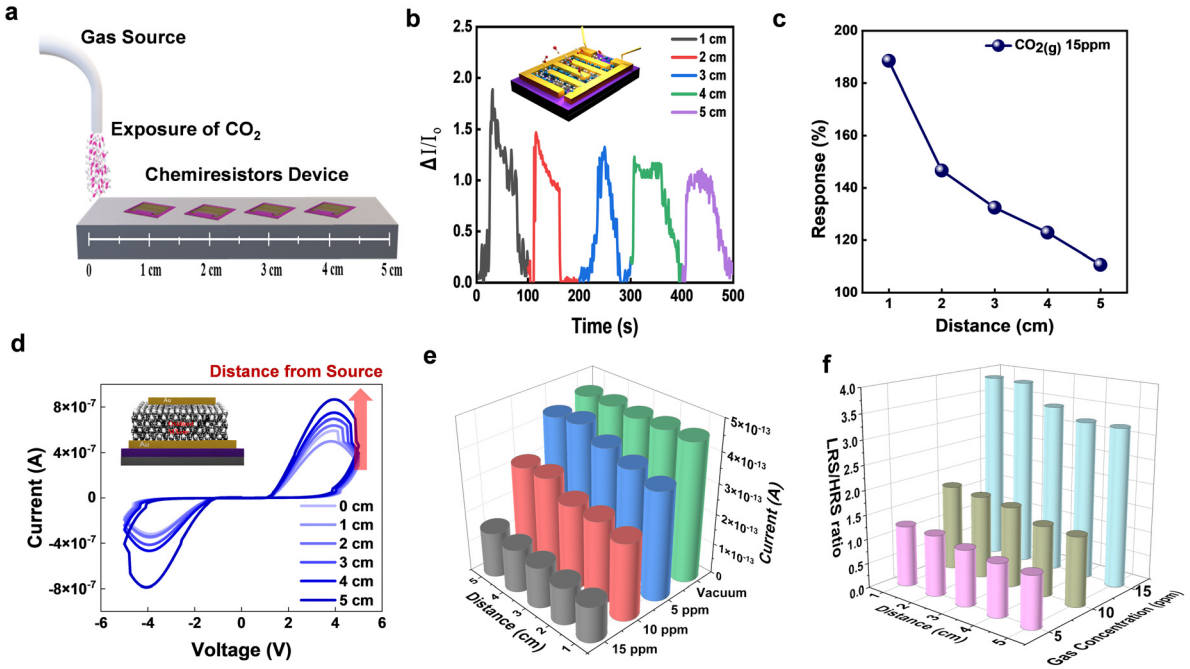

Fig. 5 (a) Schematic illustration of gas sensing at varying distances. (b) Current variation ($\Delta I/I_0$) and (c) maximum response of the oxidized MXene chemiresistive sensor to 15 ppm CO_2 at different source-to-sensor distances (1–5 cm). (d) *I–V* characteristics of the Au/oxidized MXene/Au chemiresistive memristor at varying distances with 15 ppm CO_2 exposure. (e) Histogram representation of current dependency on distance at various gas concentrations. (f) Histogram depicting the variation in the memory window as a function of gas concentration and the distance between the device and the gas source.

to decrease with increasing distance between the gas source and the sensor due to the reduced concentration of gas molecules reaching the surface of oxidized MXene surface. Similarly, Fig. 5d shows the current response of a vertical (sandwiched) Au/oxidized MXene/Au device under different gas–source-to-sensor distances and applied voltages. In this case, the current response increases with increasing distance between the gas source and the device. The actual current responses of both device configurations consistently show lower current at shorter distances and higher current at longer distances, which is consistent with typical chemiresistive behavior.

Furthermore, the variation and stability of CO_2-triggered conductance states at different distances are critical for evaluating device reliability. To assess this, we measured the conductance retention behavior at each gas–source distance under various CO_2 concentrations, recorded at a 0.1 V read voltage, as shown in Fig. S9 in the ESI.† For a more detailed understanding of the current changes with respect to distance, we extracted the current values from the distance-dependent retention measurements at each gas concentration and plotted the corresponding histograms in Fig. 5(e). A clear distance dependency was observed, characterized by a stepwise decrease in current with increasing distance. Nevertheless, distinctly separate conductance states were still observable up to a distance of 5 cm, demonstrating that the device remains operational both at close proximity and at moderate distances. This behavior was further validated by calculating the low-resistance state/high-resistance state (LRS/HRS) ratio (memory window) at each distance and for each gas concentration, as shown in Fig. 5(f). The LRS/HRS ratio increased with rising CO_2 concentration but decreased with increasing distance from the gas source. Considering both the current and memory window distance dependencies, the device exhibits significant synaptic functionality within a 5 cm range from the source. These findings underscore the critical impact of gas–source proximity on the synaptic behavior and conductance modulation of gas-triggered neuromorphic devices, emphasizing the importance of accounting for distance effects in the practical realization and scaling of artificial olfactory systems.

Fig. 6 illustrates the neuromorphic behavior of the Au/oxidized MXene/Au chemiresistive memristor under gas pulse stimulation, demonstrating its ability to replicate gas-triggered biological synaptic responses. In Fig. 6(a), a single 5 s CO_2 gas pulse was applied at a read voltage of 0.2 V, resulting in a concentration-dependent decrease in the PSC, proportional to the gas concentration. This behavior confirms the sensitivity of the device to chemical stimuli and its potential for stimulus-triggered learning. To further explore synaptic plasticity, two consecutive gas pulses (5 s pulse width with a 10 s off-time at a read voltage of 0.2 V) were applied, with the response shown in Fig. 6(b). The response to the second pulse exhibited a slightly larger current (A_2) change than the first (A_1), indicating a facilitated response an essential feature of synaptic learning behavior. To quantify this effect, paired-pulse depression (PPD) measurements were conducted by varying the inter-pulse interval from 20 to 45 s at a read voltage of 0.2 V (Fig. 6(c)).[51] The PPD index was calculated using the formula: $PPD = (A_2 - A_1)/A_1 \times 100$.

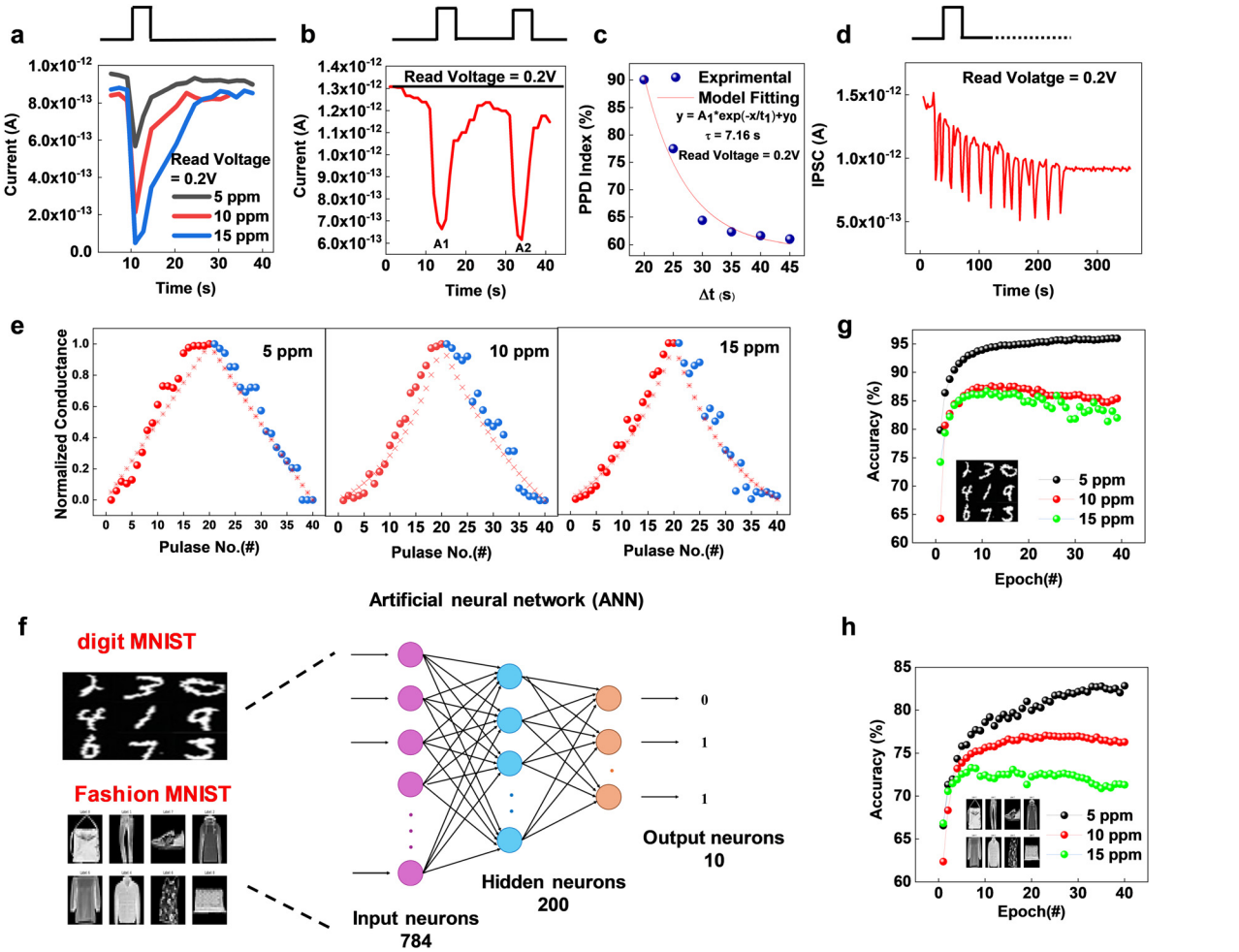

Fig. 6 (a) Postsynaptic current (PSC) response of the Au/oxidized MXene/Au chemiresistive memristor upon application of a single 5 s CO_2 pulse at a read voltage of 0.2 V, at varying concentrations. (b) PSC response following two consecutive 15 ppm CO_2 pulses with a 20 s interval between them at a read voltage of 0.2 V. (c) Paired-pulse depression (PPD) index evaluated at different inter-pulse intervals ranging from 20 to 45 s at a read voltage of 0.2 V. (d) Inhibitory postsynaptic current (IPSC) measured under 15 ppm CO_2 pulses with 5 s stimulation intervals and approximately 10 s recovery periods at a read voltage of 0.2 V. (e) Normalized conductance responses with fitted data for training artificial neural networks (ANN) using the fashion-MNIST and digit MNIST datasets under vacuum, 5 ppm, 10 ppm, and 15 ppm CO_2 conditions. (f) Schematic illustration of ANN training for fashion-MNIST classification. (g) Classification accuracy of simulated ANN models based on the synaptic behavior of the device under different CO_2 concentrations for the digit MNIST dataset. (h) Classification accuracy of simulated ANN models based on the synaptic behavior of the device under vacuum and different CO_2 concentrations for the fashion-MNIST dataset.

Here, A_1 and A_2 denote the postsynaptic currents following the first and second pulses, respectively. In Fig. 6c, the blue data points represent the experimentally measured PPD response at varying inter-pulse intervals, while the red curve corresponds to an exponential decay fit using the model $y = A_1 \cdot \exp(-x/\tau) + y_0$. The extracted time constant (τ) from the fit is 7.16 s, indicating the characteristic synaptic relaxation behavior of the device. The gradual decrease in the PPD index from 90% to 60% observed with pulse intervals of 20–45 s, supports the presence of tunable short-term plasticity. Additionally, Fig. 6(a) and (b) demonstrate that the current of the device returns to its original state after stimulus withdrawal and maintains the altered conductance after repeated exposure, corresponding to short-term and mid-term memory characteristics, respectively. To explore long-term memory behavior, 15 consecutive CO_2 gas pulses were applied with 5 s stimulation durations and approximately 10 s recovery periods at a read voltage of 0.2 V (Fig. 6(d)).[52] The initial current of 1.12 pA decreased to 0.91 pA after the pulse train (ΔI = 0.21 pA), with the altered conductance state persisting for over 100 s. This sustained response indicates the formation of long-term memory, emphasizing the strong potential of the oxidized MXene-based device for neuromorphic computing applications driven by gas stimuli.[53]

To summarize, the device exhibits volatile memory behavior: once the gas exposure ceases, the resistance returns to its initial state, confirming that the memory effect is governed by molecular adsorption and dependent on external stimuli. There is no transition to a non-volatile state; rather, both retention (Fig. 4f and g) and PSC behaviors are manifestations of the same underlying volatile mechanism under single electrical pulsing with continuous gas exposure. Although the primary focus here is on molecularly triggered memory processing,

Fig. 6a and d show that the device also demonstrates both short-term and long-term memory behaviors triggered by gas exposure, depending on the duration and frequency of gas stimulation. This switching behavior can be attributed to the slower desorption kinetics of CO_2 molecules after repeated exposure cycles. With increasing pulse repetition, CO_2 molecules may accumulate or bind more strongly to the surface, leading to prolonged modulation of conductance, which mimics long-term memory characteristics.[54] Moreover, the presence of oxygen vacancies in the oxidized MXene plays a crucial role in this behavior. These vacancies can be dynamically influenced by adsorbed CO_2 molecules. Under a low read voltage of 0.2 V, such interactions can stabilize the conductance state even after the gas pulses are stopped, contributing to a quasi-nonvolatile or long-term memory effect.

To further assess the visual adaptation capabilities of the Au/oxidized MXene/Au chemiresistive memristor, we employed the fashion MNIST and digit MNIST datasets, which contain grayscale images of 28 × 28 pixels across 10 distinct categories.[55] A total of 1024 training images and 10 000 test images were used for the simulation. The corresponding ANN architecture, depicted in Fig. 6(f), consisted of three multilayer perceptron (MLP) layers with 768 input neurons, 200 hidden neurons, and 10 output neurons. Before training, each image was flattened into a one-dimensional array and input into the MLP network. Synaptic learning was achieved through modulation of the long-term potentiation (LTP) and long-term depression (LTD) behaviors, derived from the experimental conductance values of the device. These LTP and LTD values were normalized within a 0–1 range to align with the requirements for ANN weight mapping. The normalized conductance values, shown in Fig. 6(e), were obtained under CO_2 exposures at concentrations of 5, 10, and 15 ppm. The synaptic weight updates, essential for ANN performance, were modeled using an empirical approximation based on the extracted LTP/LTD profiles, governed by the following equations.[56]

$$G^{+} = G^{+}_{\min} + \frac{G^{+}_{\max} - G^{+}_{\min}}{1 - e^{-\nu^{+}\cdot P_{\max}}} \cdot \left(1 - e^{-\nu^{+}\cdot P}\right) + \sigma \quad (3)$$

$$G^{-} = G^{-}_{\min} + \frac{G^{-}_{\max} - G^{-}_{\min}}{1 - e^{-\nu^{-}\cdot P_{\max}}} \cdot \left(1 - e^{\nu^{-}\cdot (P - P_{\max})}\right) + \sigma \quad (4)$$

here, G^{+} and G^{-} represent the normalized conductance values corresponding to LTP and LTD, respectively. The parameters ν^{+} and ν^{-} denote the nonlinearity factors associated with the LTP and LTD behaviors. P max refers to the maximum number of input pulses applied during the simulation, while σ represents the standard deviation of the Gaussian noise introduced to each conductance value. To handle negative weight values, a differential method with two devices was employed. During weight updates with the LTP or LTD conductance, only a single pulse was applied to the device for power efficiency, with the conductance changes for LTP and LTD being unidirectional. Furthermore, a reset mechanism was implemented to stabilize the training process when the conductance reached the final stage of LTP or LTD. Fig. 6(e) presents the fitted LTP and LTD curves, with the nonlinearity coefficients for LTP (ν^{+}) and LTD (ν^{-}) being 0.09 and −0.06 for 5 ppm, −0.06 and 0.05 for 10 ppm, and 0.005 and −0.02 for 15 ppm, respectively. Fig. 6(g) shows the accuracy curves of the proposed device alongside the ideal case using the digit MNIST dataset. The accuracy for digit MNIST was 95% for 5 ppm, 88.2% for 10 ppm, and 86.4% for 15 ppm, which is close to the ideal value of 97.15%. Fig. 6(h) displays the accuracy performance on the fashion MNIST dataset, yielding 82% for 5 ppm, 76% for 10 ppm, and 72.3% for 15 ppm. This optimization achieved an accuracy of 82% on fashion MNIST.

The fabricated chemiresistive device exhibits significant gas sensing capability at 5, 10, and 15 ppm concentrations of both NO_2 and CO_2, surpassing previous studies, as summarized in Table S1 (ESI†). Notably, our device demonstrates a high response of 114% for CO_2, which is the highest reported among the evaluated MXene-based sensors. Although the present devices exhibit a slow response due to molecular dynamics at the surface, future optimization efforts will focus on improving surface kinetics and material interfaces to reduce response time and enhance the applicability of the device in high-speed neuromorphic computing systems.

3. Conclusion

In summary, we have demonstrated chemiresistive memristors with analog switching, showing a significant response to CO_2 and NO_2 gases. The Au/oxidized MXene/Au chemiresistive memristor, due to the dominance of Schottky behavior compared to the ohmic behavior of bare MXene, functions as a highly sensitive neuromorphic device. The device effectively emulates key synaptic behaviors under both electrical and molecular stimuli, while maintaining analog switching. The vertically stacked memristors exhibit stable conductance retention under CO_2 exposure, tunable short- and long-term memory, and synaptic plasticity features such as potentiation, depression, and paired-pulse modulation. Molecularly induced synaptic modulation by gas pulses demonstrates long-term memory behavior, with stable responses across extended periods and varying gas concentrations and distances, positioning the system as ideal for real-world environmental or wearable neuromorphic sensing platforms. Furthermore, the synaptic characteristics of the device were leveraged for visual perception tasks through simulations with artificial neural networks trained on the fashion-MNIST and digit MNIST datasets. The high classification accuracies, achieving up to 95% and 82% for the digit and fashion datasets, respectively, underscore its practical potential for neuromorphic computing applications.

4. Experimental section

4.1. Synthesis of $Ti_3C_2T_x$ MXene

Ti_3AlC_2 powder (1 g; purity: ≥90%; Jiangsu Xfnano, China) was gradually added to a pre-mixed HF solution (20 mL; 49%, v/v; Sigma-Aldrich, USA) and stirred at 60 °C for 18 h to etch the Al

layer. Following the synthesis, the mixture was centrifuged at 3500 rpm for 5 minutes to separate the precipitate from the supernatant. The collected material was repeatedly washed with deionized water and ethanol until the pH rose above 6, ensuring removal of residual ions. A second centrifugation at 3500 rpm for 30 minutes was performed to further purify the colloidal solution. The final $Ti_3C_2T_x$ MXene product was then dried in an oven at 60 °C for 24 hours to yield powdered MXene.

4.2. Synthesis of oxidized MXene

The synthesized $Ti_3C_2T_x$ MXene was gradually introduced into a solution comprising 50 mL of deionized water and 0.3 mL of diluted hydrogen peroxide, followed by stirring at ambient temperature for 10 min. The resulting dispersion was then subjected to hydrothermal processing at 180 °C for 12 h. To prepare the oxidized MXene sensor, the oxidized MXene powder was dispersed in 1 mL of dimethyl sulfoxide (DMSO) (≥99.9%, v/v; Sigma-Aldrich, USA), sonicated for a specific duration, and stirred at room temperature for 24 h.

4.3. Fabrication of oxidized MXene chemiresistive gas sensor device

The SiO_2/Si (300 nm, 1 × 1 cm) substrate was sequentially cleaned by ultrasonication in acetone, isopropyl alcohol, ethanol, and deionized water for 10 min. Using a micropipette, 100 μL of the oxidized Mxene colloidal suspension was drop-cast onto the cleaned SiO_2/Si substrate and allowed to dry. For sensor completion, electrodes were deposited onto the substrate *via* electron beam evaporation at a vacuum pressure of 1×10^{-6} torr, using 100 nm of gold. The sandwiched Au/oxidized MXene/Au chemiresistive memristor was fabricated by first depositing a 100 nm thick gold bottom electrode onto a SiO_2/Si substrate *via* electron beam evaporation under a vacuum of 1×10^{-6} Torr. Subsequently, 100 μL of the oxidized MXene colloidal solution was drop-cast onto the substrate. After drying, a 100 nm thick gold top electrode was deposited using a circular shadow mask with a diameter of 200 μm, thereby forming the sandwiched device structure.

4.4. Material characterization

To analyze the structure and properties of MXene and oxidized MXene, several techniques were employed, including SEM-EDS (Thermo Apreo S), TEM (FEI TF30ST), XRD (Bruker D8 Advance A25 Plus; 2θ = 5°–90°), XPS (Thermo Fisher Scientific NEXSA G2), and Raman spectroscopy (MICRO LabRAM HR).

4.5. Electrical and gas sensing performance measurements

Electrical characteristics were measured using a Keithley-4200 semiconductor parameter analyzer within a drain voltage sweep range from −10 V to +10 V for both MXene and oxidized MXene. Gas sensing performance was assessed at ambient temperature in a vacuum chamber, with varying gas concentrations. Gas responses to CO_2 (g) and NO_2 (g) were calculated using $R = \frac{|I_g - I_a|}{I_a} \times 100\%$, where I_a and I_g denote the sensor currents in air and target gas, respectively. N_2 (g) was initially injected to establish a baseline before applying the target gases for 50 s, followed by a 50-s recovery period. Current measurements were recorded in real-time during gas exposure, and N_2 (g) was purged for 30 s before reintroducing the target gas. All measurements were conducted at ambient temperature, and gas concentrations were controlled using a mass flow controller.

Author contributions

S. S. K., M. A., and J. P. prepared the materials for most experimental measurements and analyzed the results. S. S. K., M. A., and J. H. P. conceived and designed the study. S. S. K. J. P., F. O. M., and I. G. D. assisted with physicochemical characterization and electrical measurements. S. S. K., M. A., and J. H. P. prepared the manuscript. All authors discussed the results and commented on the manuscript. All authors revised and commented on this manuscript. S. Y. N. and J. H. P. supervised and sponsored the study.

Data availability

The authors confirm that the data supporting the findings of this study are included within the article and its ESI.† Additional raw data are available from the corresponding author upon reasonable request.

Conflicts of interest

There are no conflicts to declare.

Acknowledgements

This study was supported by the National Research Foundation of Korea (NRF) grants funded by the Government of the Republic of Korea (RS-2023-00275300). This research was supported by Basic Science Research Program through the National Research Foundation of Korea (NRF) funded by the Ministry of Education (RS-2020-NR049575). Raman spectroscopy (MICRO LabRAM HR) for material characterization was performed at Gyeongsang National University.

References

1 Q. Zhang, C. Tian, A. Wu, Y. Hong, M. Li and H. Fu, *J. Alloys Compd.*, 2013, **563**, 269–273.
2 A. Molina, V. Escobar-Barrios and J. Oliva, *Synth. Met.*, 2020, **270**, 116602.
3 S. Kumar, G. Meng, P. Mishra, N. Tripathi and A. G. Bannov, *Mater. Today Commun.*, 2023, **34**, 105045.
4 J. Kim, W. M. Berelson, N. E. Rollins, N. G. Asimow, C. Newman, R. C. Cohen, J. B. Miller, B. C. McDonald, J. Peischl and S. J. Lehman, *Environ. Sci. Technol.*, 2025, **59**, 3508–3517.
5 I. Manisalidis, E. Stavropoulou, A. Stavropoulos and E. Bezirtzoglou, *Front. Public Health*, 2020, **8**, 14.

6 J. Z. Ou, W. Ge, B. Carey, T. Daeneke, A. Rotbart, W. Shan, Y. Wang, Z. Fu, A. F. Chrimes, W. Wlodarski, S. P. Russo, Y. X. Li and K. Kalantar-zadeh, *ACS Nano*, 2015, **9**, 10313–10323.
7 J. H. Heo, M. Sung, T. Q. Trung, Y. Lee, D. H. Jung, H. Kim, S. Kaushal, N.-E. Lee, J. W. Kim, J. H. Lee and S.-Y. Cho, *EcoMat*, 2023, **5**, e12332.
8 X.-J. Huang and Y.-K. Choi, *Sens. Actuators, B*, 2007, **122**, 659–671.
9 G. Korotcenkov, *Mater. Sci. Eng. B*, 2007, **139**, 1–23.
10 H. Ji, W. Zeng and Y. Li, *Nanoscale*, 2019, **11**, 22664–22684.
11 S. Mehdi Aghaei, A. Aasi and B. Panchapakesan, *ACS Omega*, 2021, **6**, 2450–2461.
12 S. J. Kim, J. Choi, K. Maleski, K. Hantanasirisakul, H.-T. Jung, Y. Gogotsi and C. W. Ahn, *ACS Appl. Mater. Interfaces*, 2019, **11**, 32320–32327.
13 D. Li, H. Liang and Y. Zhang, *Carbon*, 2024, **226**, 119205.
14 Y. Kim, J. H. Baek, I. H. Im, D. H. Lee, M. H. Park and H. W. Jang, *ACS Nano*, 2024, **18**, 34531–34571.
15 C. Wan, P. Cai, X. Guo, M. Wang, N. Matsuhisa, L. Yang, Z. Lv, Y. Luo, X. J. Loh and X. Chen, *Nat. Commun.*, 2020, **11**, 4602.
16 S. Y. Chun, Y. G. Song, J. E. Kim, J. U. Kwon, K. Soh, J. Y. Kwon, C.-Y. Kang and J. H. Yoon, *Adv. Mater.*, 2023, **35**, 2302219.
17 H. Kang and H.-T. Jung, *ACS Sens.*, 2024, **9**, 1031–1032.
18 N. Dennler, A. van Schaik and M. Schmuker, *Nat. Mach. Intell.*, 2024, **6**, 1451–1453.
19 I. K. G. Devara, M. J. Kwon, S.-Y. Cho, D.-J. Kwon and J. H. Park, *EcoMat*, 2024, **6**, e12453.
20 C. E. Shuck, M. Han, K. Maleski, K. Hantanasirisakul, S. J. Kim, J. Choi, W. E. B. Reil and Y. Gogotsi, *ACS Appl. Nano Mater.*, 2019, **2**, 3368–3376.
21 S. Chertopalov and V. N. Mochalin, *ACS Nano*, 2018, **12**, 6109–6116.
22 J. Tang, T. Mathis, X. Zhong, X. Xiao, H. Wang, M. Anayee, F. Pan, B. Xu and Y. Gogotsi, *Adv. Energy Mater.*, 2021, **11**, 2003025.
23 Z. Xu, R. Zhou, Q. Ma, X. Li and X. Cheng, *J. Mater. Sci.*, 2023, **58**, 4824–4839.
24 N. Hao, Y. Wei, J. Wang, Z. Wang, Z. Zhu, S. Zhao, M. Han and X. Huang, *RSC Adv.*, 2018, **8**, 20576–20584.
25 V. Natu, M. Benchakar, C. Canaff, A. Habrioux, S. Célérier and M. W. Barsoum, *Matter*, 2021, **4**, 1224–1251.
26 L.-Å. Näslund, P. O. Å. Persson and J. Rosen, *J. Phys. Chem. C*, 2020, **124**, 27732–27742.
27 A. Hermawan, B. Zhang, A. Taufik, Y. Asakura, T. Hasegawa, J. Zhu, P. Shi and S. Yin, *ACS Appl. Nano Mater.*, 2020, **3**, 4755–4766.
28 M. Han, X. Yin, H. Wu, Z. Hou, C. Song, X. Li, L. Zhang and L. Cheng, *ACS Appl. Mater. Interfaces*, 2016, **8**, 21011–21019.
29 N. B. Mullani, D. D. Kumbhar, D.-H. Lee, M. J. Kwon, S. Cho, N. Oh, E.-T. Kim, T. D. Dongale, S. Y. Nam and J. H. Park, *Adv. Funct. Mater.*, 2023, **33**, 2300343.
30 W. Y. Chen, S.-N. Lai, C.-C. Yen, X. Jiang, D. Peroulis and L. A. Stanciu, *ACS Nano*, 2020, **14**, 11490–11501.
31 A. Lipatov, A. Goad, M. J. Loes, N. S. Vorobeva, J. Abourahma, Y. Gogotsi and A. Sinitskii, *Matter*, 2021, **4**, 1413–1427.
32 J. Xu, J. Zhu, C. Gong, Z. Guan, D. Yang, Z. Shen, W. Yao and H. Wu, *Chin. Chem. Lett.*, 2020, **31**, 1039–1043.
33 M. Anayee, N. Kurra, M. Alhabeb, M. Seredych, M. N. Hedhili, A.-H. Emwas, H. N. Alshareef, B. Anasori and Y. Gogotsi, *Chem. Commun.*, 2020, **56**, 6090–6093.
34 A. Chae, S. Doo, D. Kim, T. Y. Ko, T. Oh, S. J. Kim, D.-Y. Koh and C. M. Koo, *Langmuir*, 2022, **38**, 12657–12665.
35 J. Choi, Y.-J. Kim, S.-Y. Cho, K. Park, H. Kang, S. J. Kim and H.-T. Jung, *Adv. Funct. Mater.*, 2020, **30**, 2003998.
36 C. Yuan, J. Ma, Y. Zou, G. Li, H. Xu, V. V. Sysoev, X. Cheng and Y. Deng, *Adv. Sci.*, 2022, **9**, 2203594.
37 N. Khomarloo, E. Mohsenzadeh, H. Gidik, R. Bagherzadeh and M. Latifi, *RSC Adv.*, 2024, **14**, 7806–7824.
38 L. Qian, F. Rahmati, F. Li, T. Zhang, T. Wang, H. Zhang, S. Yan and Y. Zheng, *Nanoscale*, 2025, **17**, 8975–8998.
39 A. Rawat, N. K. Chourasia, G. Rajput, Sneha and P. K. Kulriya, *ACS Appl. Nano Mater.*, 2025, **8**, 8521–8569.
40 Q. Xu, B. Zong, Q. Li, X. Fang, S. Mao and K. (Ken) Ostrikov, *J. Hazard. Mater.*, 2022, **424**, 127492.
41 P. Dipak, D. C. Tiwari, A. Samadhiya, N. Kumar, T. Biswajit, P. A. Singh and R. K. Tiwari, *J. Mater. Sci. Mater. Electron.*, 2020, **31**, 22512–22521.
42 G. Verma, A. Gokarna, H. Kadiri, K. Nomenyo, G. Lerondel and A. Gupta, *ACS Sens.*, 2023, **8**, 3320–3337.
43 J.-K. Han, M. Kang, J. Jeong, I. Cho, J.-M. Yu, K.-J. Yoon, I. Park and Y.-K. Choi, *Adv. Sci.*, 2022, **9**, 2106017.
44 S.-W. Lee, M. Kang, J.-K. Han, S.-Y. Yun, I. Park and Y.-K. Choi, *Device*, 2023, **1**, 100063.
45 J. Kang, T. Kim, S. Hu, J. Kim, J. Y. Kwak, J. Park, J. K. Park, I. Kim, S. Lee, S. Kim and Y. Jeong, *Nat. Commun.*, 2022, **13**, 4040.
46 S. Cheng, L. Zhong, J. Yin, H. Duan, Q. Xie, W. Luo and W. Jie, *Nanoscale*, 2023, **15**, 4801–4808.
47 A. Mirzaei, J.-Y. Kim, H. W. Kim and S. S. Kim, *Acc. Chem. Res.*, 2024, **57**, 2395–2413.
48 P. K. Panigrahi, B. Chandu and N. Puvvada, *ACS Omega*, 2024, **9**, 3092–3122.
49 J. Zhang, L. Liu, Y. Yang, Q. Huang, D. Li and D. Zeng, *Phys. Chem. Chem. Phys.*, 2021, **23**, 15420–15439.
50 D. Y. Nadargi, A. Umar, J. D. Nadargi, S. A. Lokare, S. Akbar, I. S. Mulla, S. S. Suryavanshi, N. L. Bhandari and M. G. Chaskar, *J. Mater. Sci.*, 2023, **58**, 559–582.
51 M. Ismail, M. Rasheed, C. Mahata, M. Kang and S. Kim, *Nano Converg.*, 2023, **10**, 33.
52 Y. Park and J.-S. Lee, *ACS Nano*, 2017, **11**, 8962–8969.
53 J.-H. Oh, J.-H. Kim, H.-J. Kim, Y.-H. Kim, K.-K. Kim and S.-N. Lee, *Adv. Intell. Syst.*, 2023, **5**, 2300350.
54 Y. Chu, H. Tan, C. Zhao, X. Wu and S.-J. Ding, *ACS Appl. Mater. Interfaces*, 2022, **14**, 9368–9376.
55 H. Xiao, K. Rasul and R. Vollgraf, *arXiv*, 2017, preprint, arXiv:arXiv:1708.07747, DOI: **10.48550/arXiv.1708.07747**.
56 S. Shim, S. Kim, D. Lee, H. Kim, M. J. Kwon, S. Cho, W. A. Lestari, J. Seo, D. Yeo, J. Na, S. S. Kundale, N. Oh and J. H. Park, *Small*, 2025, 2410892.

